Preliminary measurements with an automated compact differential absorption lidar for the profiling of water vapor

Janet L. Machol, Tom Ayers, Karl T. Schwenz, Keith W. Koenig, R. Michael Hardesty, Christoph J. Senff, Michael A. Krainak, James B. Abshire, Hector E. Bravo, and Scott P. Sandberg

The design and preliminary tests of an automated differential absorption lidar (DIAL) that profiles water vapor in the lower troposphere are presented. The instrument, named CODI (for compact DIAL), has been developed to be eye safe, low cost, weatherproof, and portable. The lidar design and its unattended operation are described. Nighttime intercomparisons with *in situ* sensors and a radiosonde are shown. Desired improvements to the lidar, including a more powerful laser, are also discussed. © 2004 Optical Society of America

OCIS codes: 010.3640, 010.7030, 140.2020, 280.0280, 280.1910, 280.3640.

1. Introduction

Water-vapor profiles in the lower troposphere are essential to characterize low-level moisture transport, which is critical for improved weather forecasts as well as climate research. Although most atmospheric water vapor occurs in the lowest 3 km, this region is not well observed.[1,2] Currently, moisture profiles for operational use are obtained primarily from twice-daily radiosonde launches or from satellite retrievals. Automated weather data are also obtained from *in situ* sensors in some commercial aircraft.[3] The infrequent radiosonde launches miss much of the variability in the low-level water-vapor field, whereas the satellite measurements are also sparse and have limited vertical resolution at low altitudes. This impedes forecasts of meteorological conditions such as precipitation amounts, where accurate and timely identification of moisture levels is important.

Lidars have been used to profile water vapor and other trace gases since the 1960s.[4] A differential absorption lidar (DIAL) uses absorption, as evidenced by reduced laser backscatter from greater distances, to measure the density of atmospheric gases. This is in contrast with a Raman lidar, which detects the wavelength-shifted return due to inelastic backscatter from selected molecules. An advantage of DIAL is that it does not require calibration, but it has stringent requirements on the laser bandwidth, wavelength, and stability, as well as an accurate knowledge of water-vapor spectroscopy around the laser wavelength. A Raman lidar requires external calibration and a high-power laser, but can have a simple transmitter design. Passive radiometric measurements at infrared wavelengths[5] can also be used to calculate profiles of humidity as well as temperature, although detailed water-vapor structure is not obtained from the data inversion process. Another technique, under development, is use of tomographic methods with arrays of global positioning system (GPS) sensors to resolve water-vapor structure.[6,7]

J. L. Machol (janet.machol@noaa.gov), C. J. Senff, and H. E. Bravo are with the Cooperative Institute for Research in the Environmental Sciences, University of Colorado and National Oceanic and Atmospheric Administration (NOAA) Environmental Technology Laboratory (ETL), 325 Broadway, Boulder, Colorado 80305. T. Ayers, R. M. Hardesty, and S. P. Sandberg are with the NOAA ETL, 325 Broadway, Boulder, Colorado 80305. K. T. Schwenz is with the Advanced Technology Division, National Center for Atmospheric Research, P.O. Box 3000, Boulder, Colorado 80307. When this research was performed, K. W. Koenig was with NOAA ETL. He is now with Infinity Software Development, 3522 Thomasville Road, Tallahassee, Florida 32308. M. A. Krainak and J. B. Abshire are with the National Aeronautics and Space Administration, Goddard Space Flight Center, Greenbelt, Maryland 20771.

Received 2 July 2003; revised manuscript received 17 December 2004; accepted 2 March 2004.

0003-6935/04/153110-12$15.00/0

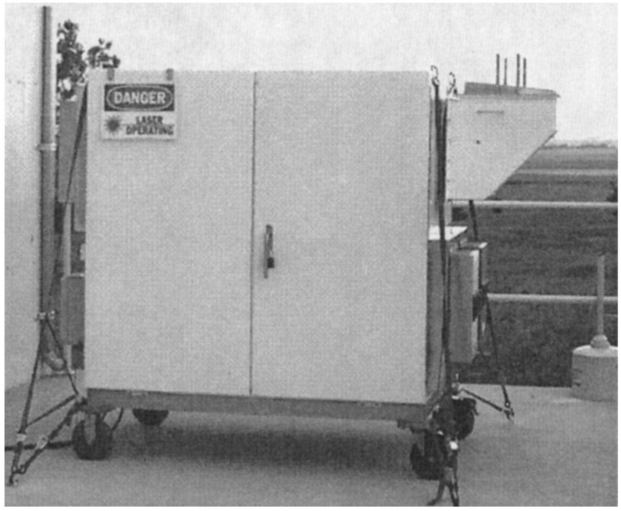

Fig. 1. Photograph of CODI.

Most existing water-vapor lidars are large, expensive, or not automated (e.g., see Refs. 8–12), although a few smaller designs have been tested.[13,14] Our goal has been to develop a compact, lower-cost, and lower-resolution DIAL that can be duplicated and deployed, ideally alongside boundary-layer radar wind profilers, in unattended arrays. Such a network could measure horizontal water-vapor transport in the lower atmosphere, which would be useful for better quantitative precipitation forecasts and long-term trends in the water-vapor field needed for climate studies.[1] The DIAL vertical profiles could be extended with column-integrated precipitable water-vapor observations obtained from either ground-based radiometer or GPS[15] methods. The ultimate commercial cost for the lidar should be around $150,000, which is less than the cost of a Vaisala LAP-3000 boundary-layer wind profiler.

CODI (for compact DIAL), an automated ground-based DIAL that continuously measures water-vapor profiles to several kilometers above ground, has been developed by the Environmental Technology Laboratory (ETL) of the National Oceanic and Atmospheric Administration (NOAA) in conjunction with the National Aeronautics and Space Administration (NASA) and the National Center for Atmospheric Research (NCAR). The lidar is in a robust, weatherproof housing with a footprint of 2.2 m × 0.9 m and is 1.8 m tall (Fig. 1). A turning mirror permits the laser beam to be transmitted at any angle from the horizontal to the vertical. The DIAL has a state-of-the-art eye-safe transmitter based on two near-infrared diode lasers. At the present time, the lidar provides nighttime water-vapor profiles with at least 15% precision for 180-m vertical resolution and ~30-min averages up to ~2-km range. In the future, with an upgraded laser, we expect that the lidar will provide similar or better measurements 24 h/day. The lidar single-channel backscatter profiles also provide cloud-base heights and qualitative measurements of aerosols. Although CODI has less resolution and range and requires longer averaging times than higher-power lidars, the temporal and spatial resolutions of this lidar are compatible with operational use.

In Section 2 we describe the theory that is used to calculate the water-vapor density from the lidar and *in situ* sensors and determine the optimum water-vapor absorption lines. In Section 3 we discuss the lidar design and operation. In Section 4 we present the lidar measurements and instrument intercomparisons that we used to evaluate the lidar. In Sections 5 and 6 we describe future system improvements and summarize the paper.

2. Theory

The basic lidar equation is[16]

$$P(R) = P_0\left(\frac{c\tau}{2}\right)\beta(R)AR^{-2}\exp\left[-2\int_0^R \alpha(r)\mathrm{d}r\right], \quad (1)$$

where P is the instantaneous received power from range R, P_0 is the transmitted peak power, c is the speed of light, τ is the pulse duration, β is the atmospheric volume backscatter coefficient, A is the effective receiver area, and α is the atmospheric volume extinction coefficient. The atmospheric backscatter is dominated by Rayleigh (elastic) scattering from gases and Mie scattering from particles. For use in water-vapor calculations, the extinction coefficient can be written as $\alpha = \alpha_{wv} + \alpha_A$ where α_{wv} is the water-vapor absorption coefficient and α_A represents all other scattering and absorption from gases and particles. The water-vapor absorption coefficient is related to the absorption cross section σ by $\alpha_{wv} = \sigma N$, where N is the number density of molecules.

Water vapor has discrete absorption lines. For water-vapor DIAL, laser pulses are transmitted at two wavelengths, one on a water-vapor absorption line and another off line. If the two wavelengths are close together and transmitted nearly simultaneously over the same path, then the aerosol scatter and non-water-vapor extinction are essentially equal for both wavelengths, and the difference between the returns at the two wavelengths is due entirely to absorption by water-vapor molecules. Thus measurement of the ratio of the backscatter at the two wavelengths as a function of range can be used to calculate the water-vapor density profile.

Assuming two closely spaced wavelengths, the water-vapor density $\rho_v(R)$ averaged over a distance ΔR at a range R is given by[17]

$$\rho_v(R) = \frac{M_{H_2O}}{N_A}\frac{1}{2(\sigma_{on}-\sigma_{off})\Delta R} \times\left[\ln\frac{P_{on}(R)P_{off}(R+\Delta R)}{P_{on}(R+\Delta R)P_{off}(R)}\right], \quad (2)$$

where M_{H_2O} is the molecular weight of water, N_A is Avogadro's constant, σ_{on} and σ_{off} are the water-vapor

absorption cross sections at the on- and off-line wavelengths, and P_{on} and P_{off} are the backscattered on- and off-line signals received by the lidar (and do not include background sky light).

The absorption cross section is $\sigma = S\Lambda$, where S is the line strength and Λ is the Voigt function. The line strength at temperature T is given by[12,18]

$$S(T) = S_0\left(\frac{T_0}{T}\right)^{1.5} \exp\left[-\frac{hcE''}{k_B}\left(\frac{1}{T} - \frac{1}{T_0}\right)\right], \quad (3)$$

where S_0 and T_0 are the line strength and the temperature at standard conditions, k_B is the Boltzmann constant, h is the Planck constant, c is the speed of light, and E'' is the lower-state energy. The line-specific values of these parameters can be found in the HITRAN tables.[19]

The Voigt function $\Lambda(\nu - \nu_0, p, T, \gamma_D, \gamma_p)$ defines the absorption line shape and depends on the frequency difference from line center $\nu - \nu_0$, the pressure p, the temperature, the Doppler half-width γ_D, and the pressure-broadening half-width γ_p. The Voigt function is a convolution of the Doppler Gaussian line shape due to thermal broadening, and the Lorentzian line shape is due to pressure (collisional) broadening.[20] The temperature and pressure used in the line-broadening calculations are extrapolated from ground-based measurements. The temperature, assumed to decrease with altitude z at the dry adiabatic lapse rate $\gamma_a = -10$ K/km, is

$$T(z) = T_s + \gamma_a z, \quad (4)$$

where T_s is the surface temperature. Assuming hydrostatic equilibrium, the pressure as a function of altitude is given by[21]

$$p(z) = p_s[T(z)/T_s]^{-g/R_L\gamma_a}, \quad (5)$$

where p_s is the surface pressure, g is the gravitational constant, and R_L is the dry-air gas constant.

There are several criteria that must be considered when DIAL wavelengths are selected.[18] The line preferably should be isolated, away from absorption lines of other species, and near a region of minimal absorption, which can be used for the off-line wavelength. The chosen line should also be relatively temperature insensitive. According to Eq. (2), because the water-vapor density depends on the absorption cross section, optimal lines have $d\sigma/dT = 0$. Following the equations similar to those stated in Ref. 18 for the mixing ratio sensitivity, $d\sigma/dT = 0$ results in a ground-state energy E'', which ranges from 181 to 361 cm^{-1} at 260 K and 208 to 417 cm^{-1} at 300 K for line shapes ranging from fully Lorentzian to fully Gaussian. More careful calculations described in Ref. 22 result in E'' values ranging from approximately 150 to 170 cm^{-1} at 260 K and 175 to 208 cm^{-1} at 300 K for pressures between 1 and 0.5 atm. It should be noted[22] that the optimal values for E'' for the water-vapor mixing ratio, which depends on the absorption coefficient, are approximately twice as large as those for the water-vapor density, which depends on the absorption cross section.

For DIAL, the pointing of the laser beam must be independent of wavelength so that both wavelengths have the same transmitter–receiver path and strike the detector identically. At close ranges, below the range of full overlap, the backscatter returns deviate from Eq. (1) for two reasons.[23,24] First, the telescope secondary mirror obstructs a portion of the return light. Second, the backscattered light from the closer ranges is defocused at the focal plane and with an intensity pattern larger than the detector. In the non-full-overlap region, any slight difference between the on- and off-line beam pointing results in incorrect DIAL measurements.

For water-vapor DIAL, it is important to have a tunable laser that can access multiple absorption lines. This permits the laser wavelength to be set to a water-vapor line with optimal line strength for the atmospheric conditions; the on-line laser beam is quickly attenuated if the line strength is too high whereas the differential signal is weak if the line strength is too low. A simple guide for line selection[25] is that the two-way optical depth (OD) should be approximately one at the desired maximum range z_{max}:

$$\mathrm{OD} = 2N\sigma z_{max} \approx 1. \quad (6)$$

A useful feature of DIAL is that, with use of appropriate-strength lines, nearly identical signal-to-noise-ratios can be obtained for profiles measured in high- and low-moisture environments.

For validation, the DIAL measurements were compared with the water-vapor density calculated from the temperature and relative humidity (RH) measured at *in situ* sites. Given the RH as[26]

$$\mathrm{RH} \approx 100\,\frac{e}{e_s} \quad (7)$$

and the equation of state of an ideal gas[26]

$$e = \rho_v R_v T, \quad (8)$$

the water-vapor density is

$$\rho_v = \frac{e_s \mathrm{RH}}{100 R_v T}, \quad (9)$$

where e is the vapor pressure, e_s is the saturation vapor pressure, and $R_v = 461$ J kg^{-1} K^{-1} is the gas constant for water vapor. The saturation vapor pressure is given by[26]

$$e_s = e_{s0} \exp\left[\frac{L}{R_v}\left(\frac{1}{T_0} - \frac{1}{T}\right)\right], \quad (10)$$

where $e_{s0} = 611$ Pa is the saturation vapor pressure at $T_0 = 273$ K and $L \approx 2.5 \times 10^6$ J/kg is the latent heat of vaporization. A slight temperature dependence of L leads to <2% error in the *in situ* values of ρ_v; this error could be reduced in the future by use of a more detailed calculation.

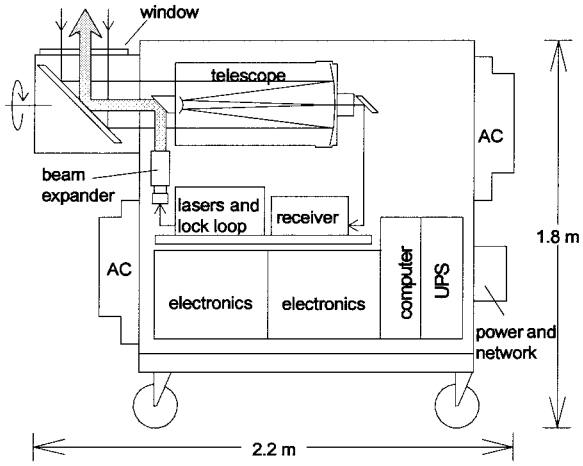

Fig. 2. Schematic of CODI. UPS, uninterruptible power supply.

Water-vapor density measurements are presented in this paper. From the equation of state for dry air, the conversion factor from water-vapor density to mixing ratio is 1.05 kg/m^3 at typical conditions in Boulder, Colorado, of 830 mbars and 276 K.

3. System Design

CODI was designed to be low cost, compact, eye safe, and automated. The lidar is housed in a weatherproof cabinet on wheels. Figure 2 is a diagram of the lidar. A diode-laser-based transmitter was chosen because it is small, rugged, and low cost. The transmitter uses an infrared continuous-wave (cw) distributed-feedback (DFB) diode laser to seed a pulsed diode flared amplifier. The receiver is based on a 35-cm-diameter telescope and photon-counting detection. All of the mirrors in the system are gold coated. The specifications for the lidar are given in Table 1.

Table 1. Lidar Specifications

Parameter	Specification	Requirement
Transmitter		
Seed laser	823-nm DFB	
Amplifier	Diode flared amplifier	
prf	6–10 kHz	
Pulse duration	600 ns	
Transmit pulse power	0.15 mJ	
Seed temperature	~24 °C ± 0.003 °C	
Amplifier temperature	~20 °C ± 0.2 °C	
Laser bandwidth	~12 MHz	<400 MHz
Frequency stability	±80 MHz	±200 MHz
Spectral purity	>99.9%	>99.5%
Receiver		
Telescope diameter	35 cm	
Far-field field of view	180 mrad	
Filter bandwidth	160 pm	
Far-field detector	APD (EG&G)	

Table 2. Accessible Water-Vapor Lines for DIAL

Wavelength (nm)	S_0 (cm^{-1} mol cm^{-2})	E'' (cm^{-1})	ρ_v* (g/m^3)[a]
823.616	1.620×10^{-23}	212	0.5–1.5
823.689	2.419×10^{-24}	756	3–10
823.960	5.400×10^{-24}	508	2–5

[a] ρ_v* is the optimal range of water-vapor density for each wavelength.

A. Transmitter

The laser requirements for a water-vapor DIAL system are stringent. According to Ref. 9, for a water-vapor DIAL to have an overall error of <5%, the laser should have a frequency stability of ±200 MHz (±0.45 pm), a linewidth of less than 400 MHz full width at half-maximum (FWHM), and a spectral purity of >99.5%. The beam pointing must be constant as a function of wavelength so that both DIAL wavelengths have the same transmitter–receiver path. The laser must also be able to switch quickly between the on- and off-line wavelengths and have a tuning range that covers multiple water-vapor lines. With a different technique, employed in other lidars,[11] various line strengths are obtained through selection of on-line wavelengths not only at the peak but also on the side of a water-vapor line; this requires greater laser frequency stability than operating at the peak of a line.

The CODI transmitter is based on an amplified infrared diode laser.[27,28] The laser, amplifier, first optical isolator, associated optics, and some electronics are housed in a small (16 cm × 22 cm × 9 cm) box with antireflection-coated windows and a 12-mm-thick invar base. In humid conditions, the box can be purged with dry air so that condensation does not damage the chilled amplifier by causing backreflections.

The seed laser is a single-mode linearly polarized cw DFB laser manufactured by Sarnoff Corporation for NASA. The 823-nm wavelength region was chosen because it has a number of moderate-strength water-vapor lines with minimal continuum absorption (from the wings of strong lines). The laser manufacturing process determined the actual wavelength tuning range of approximately 800 pm near 823 nm; some wavelengths around 816 and 818 nm are also available due to mode hops. According to the manufacturer, the DFB linewidth is approximately 12 MHz FWHM.[29] Measurements with a Micron Optics fiber Fabry–Perot tunable filter demonstrated that the laser bandwidth is on the order of 26 MHz or less.

The transmitter can access three useful water-vapor lines (823.616, 823.689, and 823.960 nm) of varying line strengths. As shown in Table 2, each of these lines is appropriate for a different range of atmospheric conditions with the optimal water-vapor densities in the range of 0.5–10 g/m^3. The corresponding relative humidity (RH) ranges from 5 to >95% at 10 °C and from 2 to 42% at 25 °C. Only the

line at 823.616 has minimal temperature sensitivity as described in Section 2; this line was used for the measurements discussed in Section 4.

The DFB wavelength can be adjusted by either temperature (60 pm/°C) or current (5.5 pm/mA) tuning. Temperature tuning is used to select the general wavelength region for a DIAL measurement. Current tuning, as it is faster, is used to switch between the on- and off-line wavelengths while the temperature is held constant. The DFB current is controlled with a Melles-Griot 06-DLD-203A diode laser driver. The on-line wavelength is maintained with the lock loop described in Subsection 3.B. The frequency stability during each set of on-line pulses is better than ±80 MHz.

Although the current change is immediate, the wavelength still has a settling time because the change in laser power causes a slight change in laser temperature. To accelerate the settling, the current is overdriven on each change of wavelength. This decreases the settling time from 20 to 3.5 s for the 8-mA adjust between the on- and off-line wavelengths. For a current change from I to $I + \Delta I$, with the computer-controlled overdrive algorithm we initially set the current to $I + 2\,\Delta I$ and then step it down to $I + \Delta I$ in five equal steps with 500-ms delays between each step and a final delay of 1 s.

The DFB lasing threshold is 33 mA and the output power is 21 mW at the maximum current of 100 mA. The laser is usually operated near 90 mA with approximately 17 mW of output power. The DFB has far-field divergence angles of 19 and 39 deg. The laser beam is approximately collimated with a 2.75-mm focal-length (FL) Geltech aspheric lens and then passes through a 60-dB optical isolator that prevents destabilizing backreflection. The 60% transmission of the isolator is adequate because the amplifier saturates with seed laser power above 7 mW. Four percent of the cw beam is deflected to the frequency lock loop described in Subsection 3.B, while the remainder is coupled into the flared amplifier with another 2.75-mm FL lens. Figure 3 shows a schematic of the lidar optics.

To reduce temperature-induced drift in wavelength and beam pointing, the DFB and its collimating lens are mounted on the same temperature-controlled copper block. To permanently mount the lens, it was aligned atop a 2-mm-diameter glass rod and sphere in front of the laser and then affixed with ultraviolet-curing epoxy. Given the strong temperature sensitivity of the laser, the laser temperature of approximately 24 °C must be held stable to within several millikelvins. A thermoelectric cooler (TEC) chills the side of the copper block holding the laser. The heat from the outer side of the TEC is extracted with a flexible copper Thermacore heat pipe that is press fit into copper plates. The heat pipe carries the heat outside of the laser box to another pair of copper plates, which are attached to aluminum fins. The laser TEC is controlled by a Thorlabs TEC2000. Because this temperature control drifts slowly, the locking optics are automatically realigned periodically, as described in Subsection 3.D.

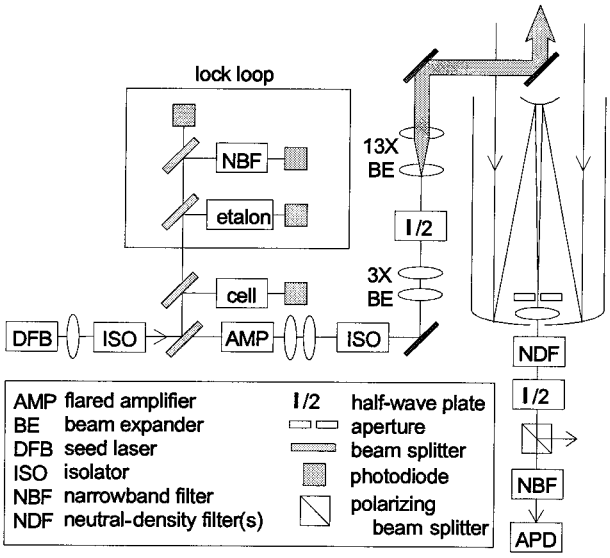

Fig. 3. Optical layout of the lidar.

A single-pass pulsed flared amplifier diode (from an SDL 8630) is used to pulse the output and to increase the laser peak power. As a single-pass single-longitudinal-mode waveguide, the amplifier output retains the seed wavelength and has constant beam pointing independent of the wavelength. The flared gain region permits a constant power density as the power increases through the amplifier. Because the amplifier is peak power limited to 0.5 W, the mean output power is maximized with long pulse lengths and a high pulse repetition frequency (prf). The constraints are that longer pulse lengths correspond to less range resolution and that higher prfs reduce the maximum range, which is determined by the spacing between two laser pulses. In general, the lidar is operated with 600-ns pulses (which corresponds to a minimum range gate of 90 m) and a prf of 8 kHz (which corresponds to a range of 18.75 km). The system can be operated at higher prfs, but then backscatter off of high clouds from the previous light pulse can appear in the pretrigger (background) data region or even in the low ranges of the next profile. For horizontal measurements at 10 kHz, there are often noticeable atmospheric returns in the off-line profile in the background region.

The amplifier is operated at 1.2 A and 20 °C. The amplifier output power increases slightly with lower temperatures. The amplifier temperature is chosen such that it remains above the dew point and is controlled to 1 °C with the Melles-Griot driver. The astigmatism of the amplifier results in a 200-mm axial separation of the tangential and sagittal beam waists. The output beam is circularized with a 2-mm FL Geltech aspheric lens and a 25-mm FL cylindrical lens. The aspheric lenses on each side of the amplifier are mounted in modified fiber positioners (New Focus 9016). The amplified pulses contain

broadband (25-nm bandwidth) amplified spontaneous emission with a magnitude of 1% of the laser power.[30] The narrowband filter in the receiver reduces the detected amplified spontaneous emission to a factor of 6×10^{-5} of the laser power. This equates to a spectral purity of ~99.994%.

After the laser box, the laser beam passes through another 60-dB optical isolator to protect the amplifier. This second isolator is outside of the laser box to separate the two isolators so that their magnetic fields do not interfere. After this isolator, the laser-pulse energy is 0.2 mJ, corresponding to an average power of 1.4 mW. The laser beam is then expanded to make the lidar eye safe. The maximum-allowable average power density at 823 nm with 6-kHz pulses is 0.56 mW/cm^2.[31] The beam passes through a 3× expander and then a custom 13× expander manufactured by CVI. The final transmit beam is approximately 40 mm in diameter.

A 76 mm × 108 mm elliptical flat turning mirror is mounted on the back of the receive telescope secondary mirror. The overlap of the transmit and receive paths is adjusted by two computer-controlled New Focus motorized micrometers on the back of the mirror mount. In the range of full overlap, it can be seen from Eq. (1) that the logarithm of a horizontal aerosol return $P_h(R)$, corrected for range $Z(R) = \log[R^2 P_h(R)]$, is constant assuming minimal absorption and constant backscatter. With the laser at an off-line wavelength, the overlap is adjusted so that $Z(R)$ is constant in the range of full overlap.

The final turning mirror is a 381 mm × 533 mm × 6.4 mm gold-plated (Tucson Optical Research Corporation) elliptical flat mirror used by both the transmit and the receive beams. The mirror substrate was cast by Wangsness Optics with ribs on the back and weighs 4.75 kg; this is 79% lighter than a solid flat of the same dimensions. This mirror is in a rotatable motorized housing that can be computer controlled and that permits the laser beam to be transmitted at any angle around one axis. The lidar is not run in a scanning mode because of the long averaging times. The mirror housing has a 12-mm-thick, 406-mm-diameter BK7 window, antireflection coated on the inside.

B. Lock Loop

To lock the laser to the correct on-line wavelength, CODI uses an edge technique with an etalon that has been calibrated to a water-vapor absorption cell measurement. The air-spaced etalon, custom manufactured by CVI, has a 30-GHz free spectral range, a 20-mm clear aperture, and spacers made of Corning ultra-low-expansion ceramic glass. The temperature expansion coefficient of the spacers is less than 30 parts per billion/K corresponding to a frequency change of less than 10.8 MHz/K. Because the interior lidar temperature is stable to better than ±1 °C, the etalon frequency is stable to ±10 MHz. The water-vapor absorption is directly measured in a 36-m path-length multipass cell (New Focus 5611) that was evacuated and then filled with water vapor to the vapor pressure. For the three water-vapor absorption lines that were used, the cell absorption was in the range of 8–30%.

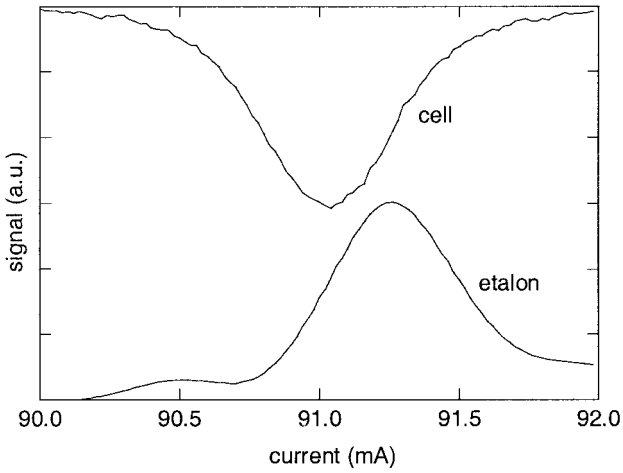

Fig. 4. Typical water-vapor cell and etalon transmission traces used in the laser wavelength lock loop.

To prepare to monitor the wavelength while taking DIAL data, the lidar first scans the laser 11 pm (2 mA) across the water-vapor line. Four photodiodes (UDT Sensors UDT-555) monitor the direct laser power as well as the transmission through the water-vapor cell, the etalon, and a narrowband filter. Because the laser power increases with current, the direct power measurement is used to normalize the other three signals. A five-point gliding average is used to smooth the cell transmission signal before calculating the maximum absorption.

After the laser scan, the etalon is rotated by the computer so that the half-height of the etalon transmission curve is at the peak of the water-vapor absorption, as shown in Fig. 4. This alignment procedure is described in more detail in Subsection 3.D. During the DIAL measurements, the laser is locked on line to the calibrated edge of the etalon transmission instead of directly to the water-vapor absorption. Locking to the etalon is faster because the etalon transmission is cleaner, and the slope provides directional information for the tuning. The laser wavelength is relocked to the etalon transmission with slight current adjustments each time the wavelength is switched on line. The etalon is automatically realigned with the water-vapor cell every 30 min to compensate for a slow (multihour) drift of the laser temperature controller.

If the laser wavelength ever drifts out of the etalon transmission peak, the lock loop also uses the transmission through a custom narrow-pass filter (Barr Associates). With a bandwidth of 230 pm, the filter transmission is roughly linear over the 11-pm scanning range and can be used by the computer to reset the laser wavelength to overlap the etalon transmission.

The off-line wavelength is obtained by switching the current by 8 mA (44 pm) from the peak of the

water-vapor line. Because this shift is more than four times the absorption line half-width (~10 pm), the transmission spectrum is fairly flat near this wavelength and no further control is needed for the off-line wavelength.

For DIAL operation, the averaging times before the wavelengths are switched are usually chosen to be 45 s on line and 10 s off line. Although the atmosphere is changing on faster time scales, the overall long averaging times of tens of minutes make it acceptable to switch wavelengths at a slow rate for these preliminary measurements. The slow rate improves the system's duty cycle because of the 3-s settling time each time the wavelength is switched. The ratio of on-line to off-line averaging times is chosen so that the signal-to-noise ratios are equal at 2 km. In the future, when the lidar is upgraded, the laser design will permit the wavelength to be switched after each pulse so as to reduce errors related to atmospheric inhomogeneities.

C. Receiver

The main receiver components are the telescope, filters, and an avalanche photodiode (APD). The lidar receiver telescope is a 35-cm-diameter $f/11$ Schmidt–Cassegrain (Celestron C14) with a corrector plate and gold-coated mirrors. The telescope is mounted horizontally in the lidar housing. The focus of the telescope is in the neck of the telescope, 82 mm from the exit. At the focus of the telescope the light passes through a 400-mm aperture that defines the field of view to be 180 mrad. This is the far-field channel. The near-field channel with a 1-mm aperture and a Hamamatsu H7421-50 GaAs photomultiplier tube (PMT) detector is currently not installed. The light is recollimated to a 5-mm-diameter beam with a 50-mm FL doublet lens and then passes through a very narrowband (160-pm) filter (Barr Associates) with 50% transmission. The narrowband filters in the receiver and lock loop are manually readjusted when the on-line wavelength is switched to a different line.

Following the narrowband filter, the receive beam is contained in a lightproof shield and is focused with a 50-mm FL doublet lens onto an EG&G SPCM–AQR single photon-counting APD with an active-area diameter of 689 mm. The APD has a dark count rate of 1400 counts/s (cps) and a quantum efficiency of 25% at 825 nm.

To avoid exceeding the APD dynamic range of approximately 3 million cps, three neutral-density filters and a shutter can be moved into the receiver path to moderate high background light. The elements are mounted in computer-controlled New Focus 8892 motorized flippers. The filters have optical densities of 0.4, 0.25, and 0.8.

The lidar uses a polarizing beam splitter in the receiver to discard approximately half of the background skylight. A pair of half-wave plates, one in the transmitter path and one in the receiver, allow the polarization angle to be optimized for skylight reduction while the laser backscatter is still detected. The receiver polarization is set to minimize the sky background, and the transmitter polarization is then aligned to match the receiver. The beam splitter can be removed if the lidar beam traverses a depolarizing atmosphere. The wave plates are mounted in motorized New Focus 8401 rotation stages and can be computer controlled.

D. Automation

The lidar is fully automated for unattended operation. An internal computer, used for data acquisition and automated alignments, is connected via an ethernet connection to an external-control computer that permits remote operation of the lidar. The internal computer contains the photon-counting board (PCB), a data-acquisition board (Real Time Devices ADA3300), a digital clock card (jxi2 ISA-SYNCCLOCK), and a general-purpose interface bus card (National Instruments AT-GPIB/TNT). Both computers use QNX 4.25 operating systems.

A function and delay generator, custom built at ETL, produces pulses at the 6–10-kHz prf to initiate data taking by the PCB and to control the amplifier. The PCB, designed at ETL, sums photon counts from the receiver detector(s) into range gates. Each function generator pulse signals the PCB to begin taking data. Then, after a delay of 14.6 ms, the amplifier current driver, a modified Directed Energy LDX-100, is triggered to produce a light pulse. For measurement of the background light, the delay provides a 2190-m-long pretrigger region before the laser pulse.

The general computer procedure is as follows. A main on-screen control panel allows the user to set many parameters such as integration times and locking tolerances. From this control panel the operator can press one button that automatically turns on all of the lidar electronics and lasers. A second button begins the DIAL data-taking sequence, which consists of locking the laser to the on-line wavelength and taking data and then switching to the off-line wavelength and taking data. After setting the laser to the on-line wavelength, the computer examines the etalon transmission and then slightly adjusts the laser current if needed. The profiles measured by the APD are summed initially by the PCB. Prior to each wavelength shift, the summed counts are read from the PCB to the computer where they can be plotted and written to a file.

The etalon and cell transmission are scanned every 30 min to check the etalon alignment. If the etalon needs realignment, it is rotated with New Focus Picomotors. The movement of the Picomotors is not repeatable and varies as much as 50% for a given number of requested steps. To adjust the etalon, the laser wavelength is temporarily set to the estimated correct location of the transmission maximum. Then the etalon transmission is monitored while the Picomotor is stepped in small increments. After the transmission peak is passed, the Picomotor is stepped back one increment. The etalon and cell transmission are then rescanned to verify their correct alignment.

The computer also controls the motorized flippers that contain the neutral-density filters and a shutter in case of excessive light. Filters are lowered when the APD signal level in any bin exceeds 51% of the maximum count rate, and they are raised when the signal falls below 18% for more than 3 min. If the shutter is closed because of high light levels, it is not raised again for 7 min.

The computer continuously monitors and displays the status of many system variables such as the laser interlocks, the detector count rates, and the ac power, updating the displayed values every 4 s. The lidar's internal temperature and humidity are monitored with an Omega HX93. If any of certain user-defined thresholds are exceeded, a lidar shutdown procedure is initiated. The laser and amplifier also have an electronic interlock box that monitors several variables such as TEC temperatures and that also shuts off the lasers if needed.

The computer runs many side processes. The time on the digital clock card is periodically updated from the lidar's GPS unit. There are also control windows that allow a user to write data files, move the etalon, or adjust the final transmitter mirror. Other windows display the atmospheric lidar returns and the photodiode signals.

E. Enclosure

Other than the external-control computer, the lidar is completely contained in a weatherproof housing. The basic enclosure, manufactured by Erpel Design Corporation, is 1.45 m high by 1.55 m long by 0.91 m wide with double doors on the two larger sides. The box has 3-mm-thick aluminum walls and is mounted on 19-cm-diameter polyurethane wheels. The exterior is white for low heat absorption. The lidar is insulated with several layers of Reflectix, a foil-coated insulating bubble pack.

The lidar uses three 20-A, 110-V power lines, two for the air conditioners (ACs) and one for the lidar electronics. An uninterruptible power supply, manufactured by Energy Technologies, Inc., serves to filter the current to the computer and other electronics and to maintain system operation in case of a power failure. Because of the limited charge life of the uninterruptible power supply battery, after several minutes of battery-powered operation, the computer shuts down the lidar.

Two Electrografics 1500-Btu solid-state ACs are mounted on each end of the lidar. They chill with TECs, heat resistively, and are controlled with a Chromalux 2110 temperature controller. Temperature feedback is provided by a resistance temperature detector mounted in the middle of the housing. The ACs maintain a stable temperature (better than ± 1 °C) with no cold gusts such as occur with compressor-type ACs. Also, because they are sealed, they do not draw dust or humidity into the system. On the other hand, the four solid-state ACs are sometimes inadequate for the lidar. They are unable to maintain the internal temperature at 23 °C when the outside temperature is above approximately 29 °C. Also, each AC draws 6 A instead of the specified 4 A. Finally, the internal humidity during operation in a humid environment is inadequately controlled because of the small input–output temperature differential of 3 °C in the cooling mode.

Interior aluminum reinforcement was added to stiffen the housing. All weight-bearing areas are tied to a lightweight 6-mm-thick aluminum plate at the base of the housing. An aluminum electronics rack supports the 5 cm $\times$ 61 cm $\times$ 91 cm optical table, the telescope, and the system electronics. The enclosure base is mounted on a 7.6-mm-thick frame for strength. Wire rope isolators beneath the base plate and the polyurethane wheels dampen shocks and vibrations. The vibration isolation works well as the lidar has twice been transported 1100 km by truck and retained its alignment both times. There is room for future modifications (or miniaturization) of the system; the clean power draw is only 4 A, and there are several unused rack shelves.

The large motorized turning mirror housing is mounted on a large-diameter Kaydon precision ring ball bearing at one end of the lidar. The mirror housing can be rotated by pressing a switch on the outside of the box. For an unattended deployment, the mirror housing rotation can be computer controlled.

4. Measurements

A. Data Analysis

The lidar data analysis is done with C programs on a laptop computer with a Linux operating system. Because of the small amount of data, processing is simple and fast; 12 h of data are analyzed in approximately 1 s. Data are transferred from the QNX computer with a Zip disk. Real-time processing could easily be added in the future.

The raw DIAL data consist of pairs of on- and off-line profiles that were electronically summed by the PCB and then transferred to the computer at the end of each wavelength-switching cycle. The PCB, which was designed for another lidar, produces 30-m (200-ns) gates that are spatially averaged later. The PCB records a profile of 256 gates, which correspond to a 7680-m range. Each profile consists of 2190 m of background (pretrigger) data, followed by the laser pulse and then the first 5490 m of atmospheric returns.

Analysis of the atmospheric data consists of detector correction, background subtraction, averaging, and application of the DIAL equation. The detector-correction factor, provided by the manufacturer, is needed at high count rates when a second photon might strike the detector before it has recovered from a first photon. For the APD, the detector dead time is 83 ns, resulting in a correction factor that ranges up to 1.46 at 3×10^6 cps. After the detector correction is applied, the background data in the pretrigger region are averaged and then subtracted from the entire profile. Finally, the raw data are block aver-

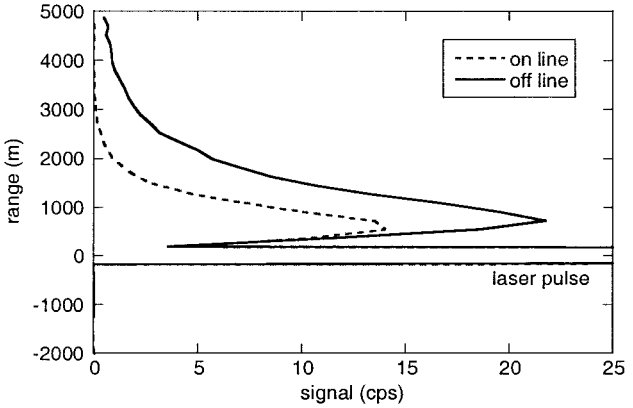

Fig. 5. On- and off-line nighttime horizontal atmospheric returns. These measurements were made at 20:24 (local time) on 3 February 2003 and calculated with 180-m, 30-min averaging and background subtraction.

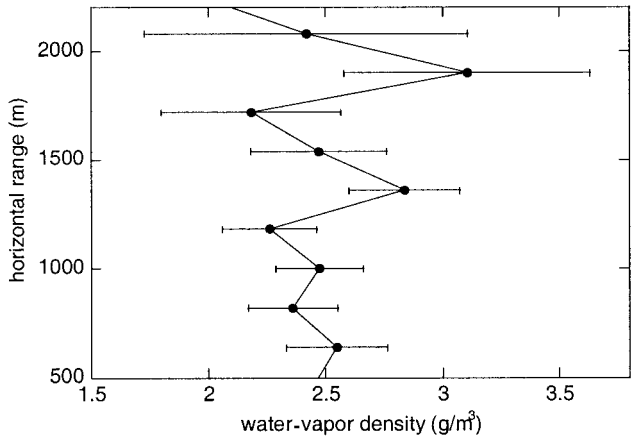

Fig. 6. Horizontal water-vapor profile recorded at 20:24 (local time) on 3 February 2003 calculated with 180-m, 30-min averaging.

aged in space and time with typical gate size and averaging time of 180 m and 30 min.

Spatial block averaging over long ranges of nonlinear data can produce biases. Several other spatial-averaging schemes were tested, but they did not make a significant difference in the DIAL calculations. Techniques tested included linear, polynomial, and exponential fits as well as peak filtering.

Profiles of water-vapor density are obtained by application of the DIAL equation [Eq. (2)] to the averaged on- and off-line data. Adjacent range gates are used for the differential calculation, and the wings of nearby water absorption lines are taken into account. No calibration is required.

Instrument-induced noise in the water-vapor measurements is determined from an autocovariance calculation.[32] For each range gate, the autocovariance function is calculated for a time series of 1-min DIAL measurements. The atmospheric variance is the extrapolation from a five-point linear fit of the autocovariance function to zero lag. The instrumental noise variance is the difference at zero lag between the total variance and the atmospheric variance. The error for each range gate is defined as the square root of the noise variance scaled to the actual time resolution of the data. The low signal-to-noise ratio is primarily due to the low signal count rate.

There are a number of small sources of systematic errors in the lidar measurements. The etalon frequency stability and the laser linewidth, frequency stability, and spectral purity were shown in Subsections 3.A and 3.B to obey requirements such that the overall DIAL error is less than 5%. Another potential source of systematic error is the photon-counting correction factor. However, for nighttime measurements, the count rates are so low that this factor is not needed. For daytime measurements, the count rates are mostly due to the background; hence at both the on- and off-line wavelengths the same correction factor is applied, and these factors cancel in Eq. (2). As discussed in Subsection 4.B, there are also errors at low altitudes in the non-full-overlap region, but these will be eliminated with the future addition of a near-field channel.

Figure 5 shows typical horizontal nighttime atmospheric returns. These background-subtracted profiles are averaged over 30 min and 180 m. At the on-line wavelength, the faster drop in counts with altitude due to water-vapor absorption is apparent. These plots show typical maximum count rates of 10–20 cps in a 30-m gate. The laser spikes at time 0 have approximately 1000 cps. In tests where the transmit beam is blocked, there is no evidence of afterpulsing on the APD from these laser spikes.

The background count rate at night is approximately 60 cps whereas during the day it ranges upward from 1000 cps depending on the sky brightness. In its present configuration, CODI can make tolerable daytime DIAL measurements with hour-long averages under clear or gray skies, but not with the high sky background from bright clouds.

B. Intercomparisons

To evaluate the lidar, we took both horizontal and vertical nighttime profiles in Boulder, Colorado. The lidar was located at the north end of the NOAA building, 10 m above ground level, and the laser beam pointed north-northeast for the horizontal profiles. The on-line laser wavelength was 823.616 nm. Figure 6 shows a horizontal water-vapor profile, demonstrating an error of $\pm 15\%$ at a range of approximately 1.7 km on this day with 30-min and 180-m averages. The error bars on the data plots were calculated with the autocovariance technique discussed in Subsection 4.A. The maximum range generally corresponds to where the on-line count rate falls below approximately 2 cps, as can be seen by a comparison of Fig. 6 with Fig. 5.

During two all-night experiments, the DIAL measurements were compared with three ground-based sensors in town. Figure 7(a) compares the value at the 1000-m range gate of the horizontal DIAL mea-

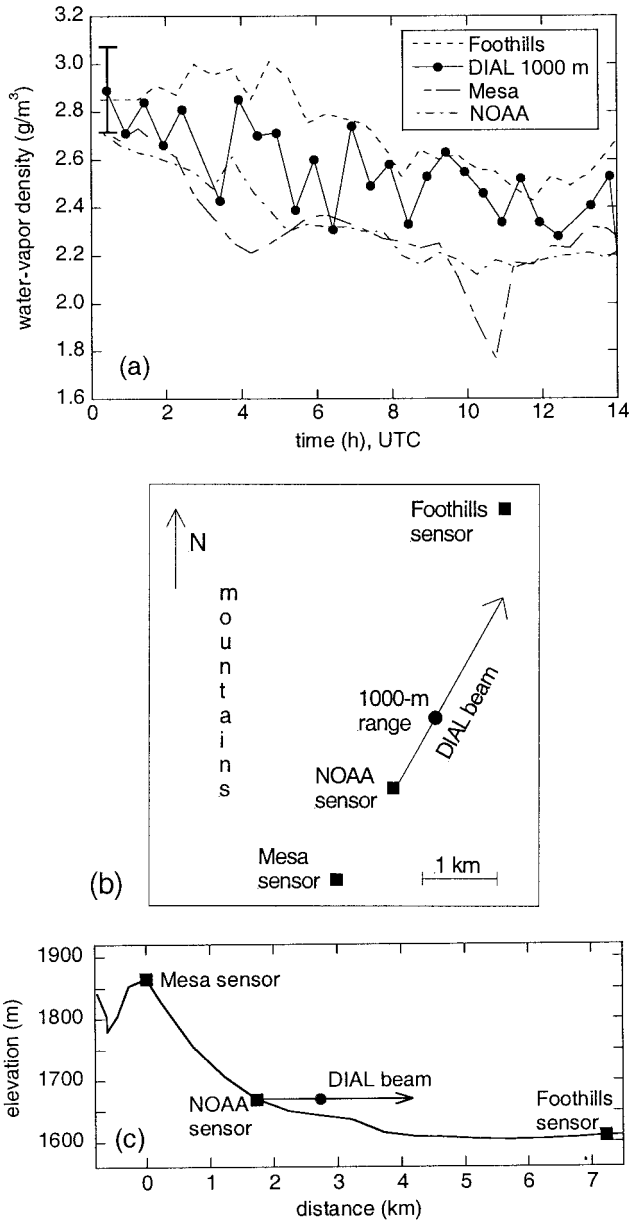

Fig. 7. (a) Nighttime comparison (14 h) of the horizontal DIAL measurements at the 1000-m range gate with ground-based *in situ* sensors. These measurements were made on 4 February 2003 UTC. The DIAL values were calculated with 180-m, 30-min averaging. The DIAL error bars are identical for all times, and so, for clarity, an error bar is shown only for the first data point. We can obtain the local time by subtracting 7 h from UTC. (b) Map of sensors and DIAL beam used in horizontal intercomparisons. (c) Cross section through Boulder showing the terrain and the locations of the three *in situ* sensors and the DIAL beam with the 1000-m range marked. The cross section is aligned with the Mesa and Foothills sensors.

surements with the *in situ* measurements. The water-vapor density at the *in situ* sites is calculated from the measured temperature and RH by Eq. (9). Autocovariance calculations show that the error in the DIAL water-vapor measurements was approximately $\pm 7\%$ for 30-min and 180-m averages. On the basis of the instruments' specifications, the errors in the water-vapor densities calculated from the *in situ* measurements were less than 4%.

Figure 7(b) is a map of Boulder showing the three *in situ* sites and the path of the lidar beam. The specifications of the *in situ* sensors are listed in Table 3. The measured water-vapor densities decrease from north to south. The Rocky Mountains, foothills, and canyon just to the west of Boulder presumably generate variability in the temperature, winds, and water vapor across the city. In addition, the *in situ* stations sample moisture at different heights, with the elevations increasing from north to south. Figure 7(c) is a cross section through Boulder showing the terrain and the locations of the three *in situ* sensors and the DIAL beam. During the experiment, the temperature ranged from -8 °C to 1 °C and the RH varied from 60 to 90%. There were light southeasterly winds throughout the evening and night until approximately 4 a.m. local time, followed by light winds from the west-northwest for the rest of the morning. The second experiment occurred on a windier night but had similar results.

Figure 8 shows a comparison of a vertical DIAL profile with the water-vapor density calculated from radiosonde measurements. To obtain a good comparison, the DIAL values were derived from 30-min averages and two sizes of range gates, 240 m at low ranges and 480 m above 2 km. The x-series Vaisala RS90-AG radiosonde was launched approximately 30 min after sunset. The profiles show good agreement to above 2.5 km. The conditions aloft were light winds (less than 6 m/s), which veered from the east to the southwest in the first 1 km and remained southwesterly up to 2 km, after which they backed to the south. At 2300 m there was a shear layer above which the winds were northwesterly. The horizontal displacement of the radiosonde from the launch site was 258 m to the west after the first vertical kilometer and 800 m to the southwest after the second kilometer.

The lidar obtains good DIAL data at ranges as close as approximately 800 m, although only the far-field optics are in place. This is approximately 400 m below the region of full overlap and indicates excellent consistency in the beam pointing between the on- and off-line wavelengths because of the single-mode waveguide structure of the amplifier.

5. Desired System Improvements

The measurements with CODI suggest several improvements to the instrument: a higher-power laser, the addition of a near-field channel, and improved climate control. For data processing, the effects of intermittent clouds on long-time-averaged data need to be considered. Together, these upgrades will make the lidar a prototype instrument capable of 24-h ground-based measurements in a variety of conditions.

A new laser source is needed for a number of reasons. Both the DFB and the flared amplifier are no longer available from the original manufacturers.

Table 3. Specifications of *in situ* Meteorological Sensors Used in Horizontal Intercomparisons

Site	Elevation (m)	Sensors	Percent Error T (°C)	Percent Error RH (at RH <90)	Percent Error in ρ_v (at $T = -2$ °C, RH = 60%)
Foothills[a]	1625	Coastal Climate Weatherpak 2000	±0.15	±2	<4
NOAA[b]	1670	Vaisala PT 100 RTD[c] (T) Vaisala Humica H (RH)	±0.1	±1	<2
Mesa[d]	1882	Paroscientific Met3A	±0.1	±1	<2

[a]The Foothills site is operated by the NCAR Atmospheric Technology Division at the NCAR Foothills Laboratory.
[b]The NOAA site is the Ground-Based GPS Integrated Precipitable Water-Vapor Demonstration Network site of the NOAA Forecast Systems Laboratory at the NOAA David Skaggs Research Center.
[c]RTD, resistance temperature detector.
[d]The Mesa site is the Suominet site SA09 at the NCAR Mesa Laboratory.

The DFB seed laser could be replaced by an external-cavity diode laser, although it has a much larger footprint. Flared amplifiers are becoming commercially available in the 800-nm region, but they still have a peak power limit of 500 mW. Substitution of a different, more powerful laser source would improve the lidar's range and resolution, especially during the day when the data are affected by bright skylight and clouds. A more powerful laser will need to be at a longer wavelength to obey eye-safety power-density constraints. A longer wavelength will also result in lower sky background light and detector quantum efficiency. Other improvements desired in a new laser are a tuning range that accesses a larger selection of good water-vapor lines and faster switching between the on- and off-line wavelengths.

Implementation of the PMT-based near-field channel will enable the lidar to obtain measurements below 800 m. The PMT has a 5-mm-diameter active area; the ~0.5-mm-diameter active area of the APD is too small for this channel. The PMT needs to be tested for afterpulsing.

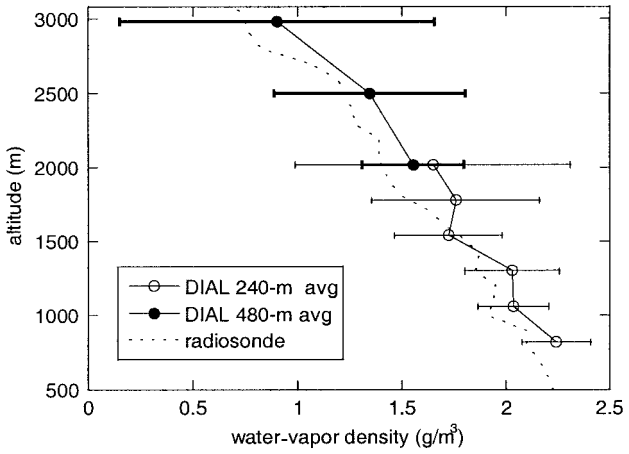

Fig. 8. Comparison of a nighttime vertical DIAL profile with radiosonde-derived values. Measurements were taken at 19:04 (local time) on 12 March 2003. The DIAL data are a 30-min average. Two vertical gate sizes are used, 240 m at lower altitudes and 480 m at the higher altitudes.

The climate control needs to be improved for conditions of high external temperature and humidity. Perhaps the addition of a layer of foam to the insulation would solve the cooling problems; otherwise, a small standard AC needs to be added. Depending on the cooling solution and whether a new laser has chilled parts, a dehumidifier might also be needed. Also, the large transmit–receive window should be heated so that condensation does not form on it.

6. Conclusions

The horizontal and vertical intercomparisons were successful and show that the DIAL works well in an unattended mode. In general, the water-vapor measurements have at least 15% precision and are processed with 30-min averaging times, 180-m range gates, and a range of approximately 2 km. Longer ranges can be obtained by an increase in the averaging. The lidar single-channel backscatter profiles also provide cloud-base heights and qualitative measurements of aerosols. The measurements demonstrate the need for several instrument improvements: a higher-power laser to permit better resolution, the addition of a near-field channel to obtain measurements below 800 m, and improved climate control. An upgraded version of CODI would be capable of 24-h ground-based water-vapor measurements in a variety of conditions and could be used in a network to measure moisture transport.

We especially thank David White for radiosonde launches and Andreas Fix and Leo Hollberg for technical discussions. We thank Raul Alvarez, Alan Brewer, James Churnside, Wynn Eberhard, Graham Feingold, Joanne George, Edith Hand, James Howell, Kevin Knott, Richard Marchbanks, Ronald Richter, Barry Rye, Ann Weickmann, and James Wilson of NOAA ETL for discussions and technical assistance. We also thank Jens Boesenberg, Donald Cornwell, Mark Flanagan, Rex Fleming, Jack Fox, John Kitching, Marzouk Marzouk, Jonathon Rall, Mitch Randall, Tim Rucker, Gregg Switzer, and Volker Wulfmeyer. The NCAR Design and Fabrication Services Division designed and machined the interior structure. Christian Grund designed the photon-counting board. This project has been funded by

NOAA ETL, NOAA Office of Global Programs, NCAR Advanced Technology Division, and NASA Goddard Space Flight Center.

References

1. W. F. Dabberdt and T. W. Schlatter, "Research opportunities from emerging atmospheric observing and modeling capabilities," Bull. Am. Meteor. Soc. **77,** 305–323 (1996).
2. T. M. Weckwerth, V. Wulfmeyer, R. M. Wakimoto, R. M. Hardesty, J. W. Wilson, and R. M. Banta, "NCAR-NOAA lower-tropospheric water vapor workshop," Bull. Am. Meteor. Soc. **80,** 2339–2357 (1999).
3. B. Moninger, R. Mamrosh, and P. Pauley, "Automated meteorological reports from commercial aircraft," Bull. Am. Meteor. Soc. **84,** 203–216 (2003).
4. R. M. Schotland, "Some observations of the vertical profile of water vapor by a laser optical radar," in *Proceedings of the Fourth Symposium on Remote Sensing of the Environment* (University of Michigan, Ann Arbor, Mich., 1966), pp. 273–283.
5. H. E. Revercomb, H. Buijs, H. B. Howell, D. D. LaPorte, W. L. Smith, and L. A. Sromovsky, "Radiometric calibration of IR Fourier transform spectrometers: solution to a problem with the high-resolution interferometer sounder," Appl. Opt. **27,** 3210–3218 (1988).
6. R. H. Ware, C. Alber, C. Rocken, and F. Solheim, "Sensing integrated water vapor along GPS ray paths," Geophys. Res. Lett. **24,** 417–420 (1997).
7. K. Hirahara, "Local GPS tropospheric tomography," Earth Planets Space **52,** 935–939 (2000).
8. J. E. M. Goldsmith, F. H. Blair, S. E. Bisson, and D. D. Turner, "Turn-key Raman lidar for profiling atmospheric water vapor, clouds, and aerosols," Appl. Opt. **37,** 4979–4990 (1998).
9. V. Wulfmeyer, "Ground-based differential absorption lidar for water-vapor and temperature profiling: development and specifications of a high-performance laser transmitter," Appl. Opt. **37,** 3804–3860 (1998).
10. D. Bruneau, P. Quaglia, C. Flamant, M. Meissonnier, and J. Pelon, "The airborne lidar LEANDRE II for water-vapor profiling in the troposphere. I. System description," Appl. Opt. **40,** 3450–3475 (2001).
11. S. Ismail, E. V. Browell, R. A. Ferrare, S. A. Kooi, M. B. Clayton, V. G. Brackett, and P. B. Russell, "LASE measurements of aerosol and water vapor profiles during TARFOX," J. Geophys. Res. **105,** 9903–9916 (2000).
12. G. Ehret, C. Kiemle, W. Renger, and G. Simmet, "Airborne remote sensing of tropospheric water vapor with a near-infrared differential absorption lidar system," Appl. Opt. **32,** 4534–4551 (1993).
13. J. A. R. Rall, J. B. Abshire, D. Reusser, and M. Humphrey, "Measurements of atmospheric water vapor using a compact AlGaAs laser based DIAL instrument," in *Conference on Lasers and Electro-Optics*, Vol. 8 of 1994 OSA Technical Digest Series (Optical Society of America, Washington, D.C., 1994), p. 196.
14. L. M. Little and G. C. Papen, "Fiber-based lidar for atmospheric water-vapor measurements," Appl. Opt. **40,** 3417–3427 (2001).
15. J. M. Duan, M. Bevis, P. Fang, Y. Bock, S. R. Chiswell, S. Businger, C. Rocken, F. Soldheim, R. H. Ware, T. A. Hering, and R. W. King, "Remote sensing of atmospheric water vapor using the Global Positioning System," J. Appl. Meteor. **35,** 830–838 (1996).
16. R. T. H. Collis and P. B. Russell, "Lidar measurement of particles and gases by elastic backscattering and differential absorption," in *Laser Monitoring of the Atmosphere*, E. D. Hinkley, ed. (Springer-Verlag, New York, 1976), pp. 71–151.
17. R. M. Schotland, "Errors in the lidar measurement of atmospheric gases by differential absorption," J. Appl. Meteor. **13,** 71–77 (1974).
18. J. Boesenberg, "Ground-based differential absorption lidar for water-vapor and temperature profiling: methodology," Appl. Opt. **37,** 3845–3860 (1998).
19. L. S. Rothman, A. Barbe, D. C. Benner, L. R. Brown, C. Camy-Peyret, M. R. Carleer, K. Chance, C. Clerbaux, V. Dana, V. M. Devi, A. Fayt, J.-M. Flaud, R. R. Gamache, A. Goldman, D. Jacquemart, K. W. Jucks, W. J. Lafferty, J.-Y. Mandin, S. T. Massie, V. Nemtchinov, D. A. Newnham, A. Perrin, C. P. Rinsland, J. Schroeder, K. M. Smith, M. A. H. Smith, K. Tang, R. A. Toth, J. Vander Auwera, P. Varanasi, and K. Yoshino, "The HITRAN molecular spectroscopic database: edition of 2000 including updates through 2001," J. Quant. Spectrosc. Radiat. Transfer **82,** 5–44 (2003).
20. R. Loudon, *The Quantum Theory of Light* (Clarendon, Oxford, UK, 1983).
21. S. L. Hess, *Introduction to Theoretical Meteorology* (Holt, Rinehart & Winston, New York, 1959).
22. E. V. Browell, S. Ismail, and B. E. Grossmann, "Temperature sensitivity of differential absorption lidar measurements of water vapor in the 720-nm region," Appl. Opt. **30,** 1517–1524 (1991).
23. J. Harms, W. Lahmann, and C. Weitkamp, "Geometrical compression of lidar return signals," Appl. Opt. **17,** 1131–1135 (1978).
24. T. Halldorsson and J. Langerholc, "Geometrical form factors for the lidar function," Appl. Opt. **17,** 240–244 (1978).
25. E. E. Remsberg and L. L. Gordley, "Analysis of differential absorption lidar from the space shuttle," Appl. Opt. **17,** 624–630 (1978).
26. R. R. Rogers, *A Short Course in Cloud Physics* (Pergamon, New York, 1983).
27. J. N. Walpole, "Semiconductor amplifiers and lasers with tapered gain regions," Opt. Quantum Electron. **28,** 623–645 (1996).
28. D. F. Welch, "A brief history of high-power semiconductor lasers," IEEE J. Sel. Top. Quantum Electron. **6,** 1470–1477 (2000).
29. N. A. Morris, J. C. Connolly, R. U. Martinelli, J. H. Abeles, and A. L. Cook, "Single mode distributed feedback 761 nm GaAs-AlGaAs quantum-well laser," IEEE Photon. Technol. Lett. **7,** 455–457 (1995).
30. *SDL-8630 Tunable Laser Diode Operator's Manual* (SDL, Inc., San Jose, Calif., 1996).
31. American National Standard for the Safe Use of Lasers, ANSI Z136.1-2000 (Laser Institute of America, Orlando, Fla., 2000).
32. D. H. Lenshow, V. Wulfmeyer, and C. Senff, "Measuring second- through fourth-order moments in noisy data," J. Atmos. Oceanic Technol. **17,** 1330–1347 (2000).